Available online at www.sciencedirect.com
ScienceDirect
International Journal of Multiphase Flow 33 (2007) 67–85
International Journal of Multiphase Flow
www.elsevier.com/locate/ijmulflow

Effect of secondary flow on droplet distribution and deposition in horizontal annular pipe flow

J.M.C. van 't Westende, R.J. Belt, L.M. Portela *, R.F. Mudde, R.V.A. Oliemans

J.M. Burgerscentrum for Fluid Mechanics, Delft University of Technology, Kramers Laboratorium, Prins Bernhardlaan 6, 2628 BW Delft, The Netherlands

Received 15 March 2006; received in revised form 12 July 2006

Abstract

In horizontal annular dispersed pipe flow the liquid film at the bottom is thicker and rougher than at the top of the pipe. A turbulent pipe flow experiencing a variation of roughness along the pipe wall will show a secondary flow. Such secondary flow, consisting of two counter-rotating cells in the cross-section of the tube, can change the distribution of the droplets inside the pipe and their deposition at the wall. Here, we compare the behaviour of the droplets (dispersed phase) with and without secondary flow, using large-eddy simulations. It is shown that the presence of secondary flow increases the droplet concentration in the core of the pipe and the droplet deposition-rate at the top of the pipe.

Keywords: Horizontal annular flow; Two-phase gas–liquid flow; Free-flight; Turbulence; LES

1. Introduction

In horizontal annular two-phase flow, the liquid-phase flows partly as a thin film along the tube wall and partly as entrained droplets in the turbulent gas core. Due to gravitational pull, the liquid film at the bottom part of the pipe usually is thicker than that at the top of the pipe. Similarly, the concentration of drops will be higher in the bottom region than in the top region of the pipe. This flow regime occurs often in transport pipes of gas and oil and in heat exchangers. An important parameter for this flow regime is the film flow-rate along the wall. When part of the pipe wall is not covered with a liquid film, corrosion of the wall can take place and heat exchange from the wall to the liquid is deteriorated, a so-called dry-out.

The gravitational pull on the liquid film results in a constant drainage of liquid from the top of the pipe towards the bottom. In order to maintain a liquid film along the entire wall of the pipe, other mechanisms have to be present to transport the drained liquid back to the top of the pipe. A number of such mechanisms have been proposed over the years, see e.g. Mols (1999):

* Corresponding author. Tel.: +31 15 278 2842; fax: +31 15 278 2838.
E-mail address: l.portela@tudelft.nl (L.M. Portela).

0301-9322/$ - see front matter © 2006 Elsevier Ltd. All rights reserved.
doi:10.1016/j.ijmultiphaseflow.2006.07.004

(1) Surface tension: curvature differences in the liquid film along the circumference induce pressure gradients in the tangential direction, 'pumping' the liquid film upwards. This effect is only important for small-diameter pipes ($D < 5$ mm for air–water systems).
(2) Secondary gas-flow: a mean flow in the cross-section of the pipe, usually manifested as multiple counter-rotating cells (see Fig. 1c), is able to drag the liquid film upwards by its tangential shear-force. Secondary flow can be induced by a varying wall-roughness, Darling and McManus (1968), by the non-uniformity of droplet concentration, Belt et al. (2005), or by the fact that the gas is flowing through an non-circular cross-section, Speziale (1982).
(3) Entrainment/deposition: droplets, mostly atomised from the thick film at the bottom part of the pipe, can deposit downstream in the top region, where they contribute to the film.
(4) Wave-spreading: large amplitude waves, being deformed by the non-uniform depth of the liquid film, tend to bend sidewards and spread over the circumference.

The effects of secondary flow on the liquid film are quite controversial. Jayanti et al. (1990) simulated a secondary flow and found its tangential shear to be insufficient to sustain a liquid film at the top of the pipe wall. In a later paper (Jayanti and Hewitt, 1996), using isolated patches of wall-roughness, they even question the existence of secondary flow in annular flow. Measurements of Dykhno et al. (1994), Flores et al. (1995) and Williams et al. (1996), however, do show the existence of secondary flow. Lin et al. (1985) made a model including all four mechanisms mentioned above; they concluded that secondary flow and entrainment/deposition are the dominant mechanisms for the film distribution.

All the work mentioned above deals with the direct effect of the secondary flow on the liquid film. However, the secondary flow can also have an indirect effect on the liquid film by affecting the distribution of the droplets and their deposition at the wall. The objective of this paper is to study how the secondary flow, induced by a variable wall-roughness, influences the dispersed-phase distribution and the deposition-rate. The study was performed by doing numerical simulations both without secondary flow and with secondary flow created with a varying wall-roughness. In our computations, the processes that drive the dispersed phase are: gravitational settling, turbulence interactions and secondary flow, Fig. 1. Gravity pulls the droplets down, thus increases the deposition at the bottom of the pipe and diminishes it at the top. The turbulence of the gas acting on the droplets, via the drag force, tends to push them towards zones of low turbulence intensity (i.e. the wall); a phenomenon known as turbophoresis, Young and Leeming (1997). Turbophoresis has no preferential deposition region and deposits the droplets uniformly along the wall, provided the turbulence intensity shows cylindrical symmetry.

The proposed effects of secondary flow are that the droplets are dragged along with its counter-rotating cells, transporting them to the top of the pipe, therefore increasing the droplet-concentration in the core and top regions of the pipe. The gravitational settling of the droplets along the wall is reduced by the secondary flow, but in the core of the pipe it is enhanced. Another possible deposition mechanism is the centrifugal effect of secondary flow: due to inertia the droplets tend to be swept outwards, depositing on the pipe wall. Similarly to turbophoresis, deposition by the centrifugal effect should occur everywhere along the circumference, but not necessarily with equal strength.

The paper is organised as follows. In Section 2, we formulate the problem and detail the major mechanisms involved. The models used in the numerical simulation of the particle-laden turbulent pipe flow and for cre-

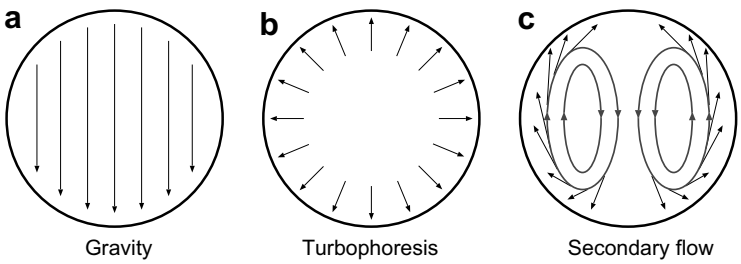

Fig. 1. Deposition mechanisms in a horizontal annular dispersed pipe flow.

ating a secondary flow are described in Section 3. The validation of these models is provided in Appendix A. In Section 4.1, the results of the secondary flow are shown, and its effects on the dispersed phase are described in Section 4.2. Finally, some concluding remarks are given in Section 5.

2. Problem formulation

Instead of simulating the liquid film, in this paper we consider a simplified situation: the gas–liquid interface is represented by a circular wall with a varying roughness, inducing a secondary flow pattern. The droplets are considered as small solid spheres and are driven by drag and gravity only, which are the most important driving mechanisms in the actual situation. To focus on the effect of secondary flow on the particles, we also neglect the effect of the particles on the flow and inter-particle interactions (i.e. we consider one-way coupling). Since there does not exist any fundamental study on the effect of the secondary flow on a dispersion of droplets in a horizontal annular flow, we deliberately kept the situation as simple as possible, leaving out all forces acting on the particles except for drag and gravity, and leaving out two-way coupling and inter-particle collisions. In this way, the effect of secondary flow itself on a dispersion is isolated, allowing a better understanding of the physical mechanisms involved. Note that including two-way coupling might change the secondary flow pattern; Belt et al. (2004) and Dykhno et al. (1994).

In a real annular flow, droplets continuously deposit onto and re-entrain from the liquid film. Once a droplet is created, we can calculate its path using the forces exerted on it. When the droplet hits the wall, it is removed from the flow. In steady state, the average rate of entrainment is equal to the average rate of deposition. The details of entrainment, however, are not known, and it is therefore not clear what boundary conditions would best represent an actual annular flow. Two extreme possibilities for the boundary conditions are: (i) absorbing wall and (ii) specular-reflecting wall. The first would represent a perfect absorbing wall without any re-entrainment, whereas the second would represent a local equilibrium between deposition and re-entrainment. In the simulations we only considered a specular-reflecting wall; particles maintain their axial and tangential momentum but reverse their radial momentum, when bouncing at the wall. Each collision with the wall is treated as a deposition event. Since the number of particles remains constant, it is easier to obtain meaningful statistical results with a specular-reflecting wall than with an absorbing wall. Note, however, that the specular reflecting wall is a rather simplistic model, and that the situation in an actual annular flow can be quite complex.

Due to turbulence–particle interactions (i.e. turbophoresis, Young and Leeming, 1997), the particles are driven to the wall and tend to cluster there. The particles that are clustered near the wall, while sliding down forced by gravity, van 't Westende et al. (2004), hit the wall frequently, and thus are a dominant factor concerning deposition in the simulations. In an actual annular flow, however, this is not the case, since the near-wall droplets are removed when depositing at the wall. In Section 4.2, we show how to identify these sliding particles amongst the depositing particles. Since the sliding particles clustered near the wall have little interaction with the gas-phase turbulence, they are referred to as passive particles, whereas the active particles still interact with the turbulence of the gas.

All the simulations are done for an air–water system in a horizontal pipe with a diameter $D = 5$ cm. In every computation, the bulk velocity, U_{bulk}, was set to about 20 m/s, corresponding to a bulk Reynolds number $Re_{\text{bulk}} \approx 65{,}000$ ($\rho_g = 1$ kg/m^3 and $\nu_g = 1.5 \times 10^{-5}$ m^2/s). The magnitude of the secondary flow velocity, U_{sf}, is roughly equal to 0.2 m/s. The diameter of the secondary flow cells, D_{sf}, is about $D/2$, resulting in an centrifugal acceleration of about 4 m/s^2, which is of the same order of magnitude as the gravitational acceleration. We did simulations with two different particle diameters: $d_p = 50$ μm and $d_p = 100$ μm, for which the terminal free-fall velocity, V_T, is 0.09 m/s and 0.35 m/s, respectively; i.e., in both cases the terminal free-fall velocity is of the same order of magnitude as the secondary-flow velocity.

3. Simulations

We use Eulerian–Lagrangian LES with the standard point-particle approach, e.g. Portela and Oliemans (2003).

For the continuous phase, the gas velocity, $\vec{u}_g$, is simulated using a large-eddy simulation (LES). The filtered continuity and Navier–Stokes equations, that are solved for the gas-phase, are,

$$\nabla \cdot \vec{u}_g = 0 \tag{1}$$

$$\frac{\partial \vec{u}_g}{\partial t} + (\nabla \vec{u}_g) \cdot \vec{u}_g = -\frac{1}{\rho_g} \nabla p + \nu_g \nabla^2 \vec{u}_g + \nabla \cdot \vec{\vec{T}}_s \tag{2}$$

with ρ_g and ν_g being the density and the kinematic viscosity of the gas-phase. The influence of the subgrid motion on the resolved gas-velocity is represented by the extra stress-tensor, $\vec{\vec{T}}_s$. The in-house code that is used for the calculations solves Eqs. (1) and (2) using a finite-volume single-phase solver with a predictor–corrector method. In the predictor part, a leap-frog method, explicit in the radial and axial directions and implicit in the tangential direction, is used for progress in time. In the corrector step, the continuity equation is enforced using the Poisson equation for incompressible flows. The time-step is determined with the Courant criterion. The stress-tensor, $\vec{\vec{T}}_s$, is computed using the standard Smagorinski model, with the Smagorinski constant $C_s = 0.1$. Van Driest wall-damping is also applied, with $A^+ = 25$. Throughout this paper, the superscript $+$ is used when a quantity is normalised with ρ_g, ν_g and the friction velocity, u_τ. More details about the single-phase solver can be found in Eggels (1994).

A staggered-grid in cylindrical coordinates is used and periodic boundary conditions are applied in the axial direction. In Fig. 2, the computational domain with the corresponding position and velocity coordinates for the axial, tangential, and radial directions is drawn. For all the simulations, the gridpoints are uniformly distributed in the tangential and axial directions, with $N_\phi = N_z = 192$. The length of the computational domain in the axial direction is $L_z = 5D$. In the radial direction the grid is stretched, using a hyperbolic-tangent function,

$$r_i = \frac{\tanh(C_1 i/C_2)}{2\tanh(C_1)} D, \quad 0 < i < N_r \tag{3}$$

using the following constants: $N_r = 32$, $C_1 = 2.45$ and $C_2 = 40$. This grid has a wall-nearest grid-point at a distance from the wall, $y \approx D/68$, a grid-spacing near the wall, $\Delta y_w \approx D/350$, and a grid-spacing in the center $\Delta y_c \approx D/32$. Note that because we are using wall-functions, the first grid-point near the wall is located in the logarithmic layer, and is at a larger distance from the wall than the near-wall grid spacing.

In order to account for the wall-roughness, the Schumann wall-function is implemented for the near-wall region, $0 < y/D < 0.015$, Piomelli et al. (1989). The boundary conditions for the grid-cells near the wall (see Fig. 3) are

$$u_{r,imax} = 0 \tag{4}$$

$$\tau_{r\phi,\mathrm{wall}} = -\rho_g \nu_g \frac{u_{\phi,imax}}{y_{imax}} \tag{5}$$

$$\tau_{rz,\mathrm{wall}} = -\rho_g u_\tau^2 \frac{u_{z,imax}}{U_{z,imax}} \tag{6}$$

$$U_{z,imax} = \frac{u_\tau}{\kappa} \ln(y_{imax}/k_{\mathrm{eff}}) + 8.5 \tag{7}$$

$$k_{\mathrm{eff}} = \max(k_s, k_{s,\min}) \tag{8}$$

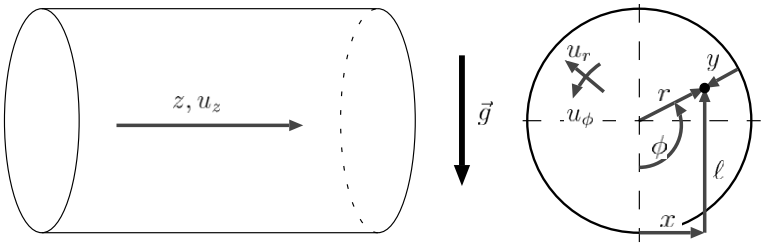

Fig. 2. Computational domain, together with position and velocity coordinates.

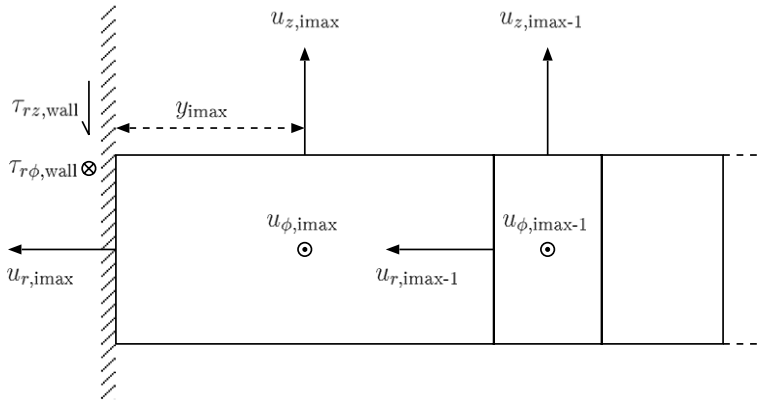

Fig. 3. Wall-shear for wall-nearest grid-cell.

$u_{r,imax}$, $u_{\phi,imax}$ and $u_{z,imax}$ represent the instantaneous radial, tangential and axial velocities and $U_{z,imax}$ the average axial-velocity at the wall-nearest grid point. The two components of the wall-shear are given by $\tau_{r\phi,\mathrm{wall}}$ and $\tau_{rz,\mathrm{wall}}$. y_{imax} is the distance to the wall for the wall-nearest grid point, κ is the von Karman constant and k_{eff} is the effective local wall-roughness. The effective local wall-roughness is equal to the actual local wall-roughness, k_s, but cannot be smaller than a minimum, $k_{s,\min}$, thus forcing Eq. (7) to match the smooth wall law of the wall for $k_s^+ \leqslant k_{s,\min}^+ = \exp(3.5\kappa)$, Jimenez (2004).

The friction-velocity, u_τ, is calculated using the Fanning friction-factor, f, which is estimated with the Churchill relation, Churchill (1977).

$$u_\tau = U_{\mathrm{bulk}}\sqrt{f/2} \tag{9}$$

$$f = 2[(8/Re_{\mathrm{bulk}})^{12} + (c_1 + c_2)^{-3/2}]^{1/12} \tag{10}$$

$$c_1 = [2.457\ln((7/Re_{\mathrm{bulk}})^{0.9} + 0.27k_s/D)]^{16}$$

$$c_2 = (37530/Re_{\mathrm{bulk}})^{16}$$

Re_{bulk} is the Reynolds number based on U_{bulk} and D. When the roughness is varied around the circumference, a local friction-factor is calculated for every tangential position, and the average of these local friction-factors is used in Eq. (9). Three simulations were performed:

- F_{sm}: Uniform smooth-wall, $u_\tau = 0.99$ m/s, $Re_{\mathrm{bulk}} = 65{,}300$,
- F_{ro}: Uniform rough-wall, $k_s/D = 0.03$, $u_\tau = 1.58$ m/s, $Re_{\mathrm{bulk}} = 64{,}000$,
- F_{var}: Varying wall-roughness, $0 < k_s/D < 0.03$, $u_\tau = 1.34$ m/s, $Re_{\mathrm{bulk}} = 63{,}500$.

Simulations F_{sm} and F_{ro} are detailed and validated in Appendix A, and simulation F_{var} is discussed in Section 4.1.

The particles are treated as point-particles and are tracked individually using non-linear drag and gravity. The drag coefficient used is

$$C_D = 24\frac{\mu_g}{\rho_g|\vec{u} - \vec{v}|d_p} + 0.44 \tag{11}$$

which gives a good approximation of the standard drag curve, Govan (1989); with $\vec{v}$ the instantaneous particle-velocity and d_p the particle-diameter. Using this drag coefficient, a terminal free-fall velocity in a stagnant medium, V_T, is calculated. In this paper, the particle-relaxation-time, τ_p, is defined as

$$\tau_p = V_T/g \tag{12}$$

Similarly to the continuous-phase, periodic boundary conditions are also applied for the particles: when a particle leaves the domain, it is re-introduced with the same velocity at the opposite side. The particles progress in

time is done with a second-order Adams-Bashforth method. According to Portela and Oliemans (2002), in our case the subgrid motion does not affect significantly the particle motion, since the timescales of the subgrid motion are much smaller than the particle-relaxation-time and the subgrid velocity fluctuations are much smaller than the grid-scale velocity fluctuations. Therefore, the influence of the subgrid-scales on the particle motion is neglected. Further details on the particle-tracking can be found in Portela and Oliemans (2003).

4. Results

4.1. Secondary flow

Darling and McManus (1968) measured secondary flow in a 10 cm diameter pipe with varying wall-roughness, using hot-wire anemometry. They used an air-flow at atmospheric conditions with bulk velocity $U_{\text{bulk}} = 13.4$ m/s, resulting in a Reynolds number of about 89,000. In their experiments, the bottom of the pipe had a hydraulic wall-roughness $k_s/D \approx 0.03$, decreasing gradually towards the top, where it becomes smooth. A secondary flow is then created such that a flow exists along the wall, from the rougher to the smoother region, and back through the center of the pipe, from the smooth wall to the rough wall, resulting in two big vortex-cells, as shown schematically in Fig. 1c.

In the simulation F_{var}, the wall-roughness is varied around the circumference similarly to the experiments done by Darling and McManus, with

$$\frac{k_s}{D} = 0.015(\cos(\phi) + 1) \tag{13}$$

Using this variation of roughness results in $u_\tau = 1.34$ m/s. In our simulations the wall-roughness is implemented using wall-functions, see Appendix A for details.

In Fig. 4 the results of simulation F_{var} are shown, averaged in the axial direction and over 140 uncorrelated fields. Fig. 4a shows the mean axial-velocity, Fig. 4b the magnitude of the secondary-flow velocity together with some streamlines, and Fig. 4c the tangential-velocity fluctuation. Since the results are essentially symmetric with respect to the vertical axis, only half of the pipe is drawn.

The maximum value of the mean axial-velocity is not in the center of the pipe, but is shifted towards the rough bottom. This is a result of the secondary flow (downwards through the center of the pipe), bringing axial-momentum from the center of the pipe to the bottom region. It thus seems as if the secondary flow 'pushes' the position of maximum axial-velocity downwards. In the literature, the presence and direction of secondary flow is usually shown via the mean axial-velocity profile. However, in general, there does not exist a one-to-one correspondence between the pattern of the secondary flow and the mean axial-velocity profile, Belt et al. (2005). In general, as shown, e.g., by Belt et al. (2004), the secondary flow is determined by the pat-

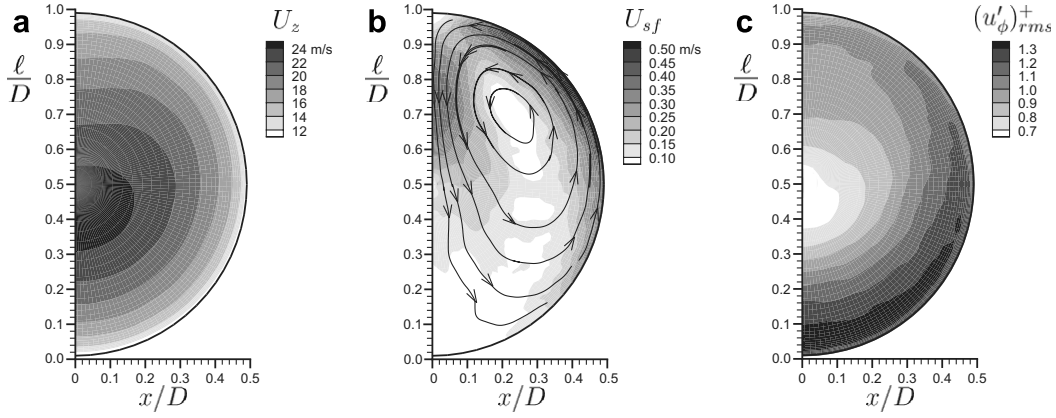

Fig. 4. Contour plots of simulation F_{var}: (a) mean axial velocity, (b) secondary-flow strength with some streamlines, and (c) tangential-velocity fluctuation.

tern of the Reynolds stresses in the cross-section of the pipe. In our case, the secondary flow consists of two symmetric cells with respect to the vertical axis, with a flow upward along the wall and downward through the center. At the bottom of the pipe the wall-shear and the Reynolds stresses are larger, Fig. 4c. As shown by Belt et al. (2004), the gradient in the tangential Reynolds-stress along the wall, shown in Fig. 4c, pushes the flow in the opposite direction (i.e., from the high towards the low values of $(u'_\phi)^+_{\mathrm{rms}}$), creating the secondary-flow pattern shown in Fig. 4b.

According to Darling and McManus (1968), there is little or no Reynolds-number effect on the mean axial-velocity profile or the secondary-flow pattern, so their results can be compared with simulation F_{var}. The friction factor of F_{var} is only 4% larger than the value reported by Darling and McManus. This indicates that a circumferential-averaged friction factor seems to be a good way of determining the global friction factor; i.e. each roughness element contributes equally to the total wall-shear.

Darling and McManus found that the tangential component of the secondary flow reaches a maximum value of 7% of the local axial-velocity, at $\phi \approx 110°$, very close to the wall ($y/D = 0.0065$). In the simulation F_{var}, the tangential component of the secondary flow reaches a maximum value of 5.2% of the local axial-velocity, at $\phi \approx 130°$, and also very close to the wall. Both the position and the magnitude of the maximum secondary-flow velocity of F_{var} are close to those of the experiments of Darling and McManus. Since it is very difficult to measure a small in-plane component of the gas-velocity very close to the wall, this might be a possible reason for the small differences. Another possible cause for the difference in the position and magnitude of the maximum secondary-flow velocity can be associated with the friction-velocity used in the simulations. In Eqs. (6) and (7), we used the average friction-velocity instead of the local one. Implementing a local friction-velocity, will increase the wall-shear difference between the bottom and the top of the pipe, and therefore will generate a stronger secondary flow. However, the difference between the two implementations of the friction-factor (average or local) is small. Since we have not found detailed experiments that favor the use of a local friction-factor, we decided to use the average friction-factor in Eqs. (6) and (7). Note that, even though the friction velocity is constant along the circumference, there exists a local variation of k_s, leading to a local variation of the wall-shear, which is the source of the secondary flow; in our case the friction velocity is a global effect associated with the pressure-gradient.

In Fig. 5 we show the radial-velocity fluctuations on the vertical axis, for the simulation without secondary flow, F_{sm}, and the simulation with secondary flow, F_{var}. For both the simulations F_{sm} and F_{var}, there exists a minimum radial-Reynolds-stress in the center and near the wall, and maxima at $y/D \approx 0.1$. The effect of the wall-roughness is clearly visible from the magnitude of the radial-velocity fluctuation, and scales roughly with u_τ. For F_{var} the radial-velocity fluctuations are larger at the bottom where the wall-roughness is larger.

The strong gradients in the radial turbulence-intensity near the wall lead to the turbophoresis effect, Young and Leeming (1997). A balance of momentum in the radial direction shows that a gradient in the radial-velocity fluctuation of the particles results in a net force in the opposite direction. Since the velocity fluctuation of the particles is determined by the velocity fluctuation of the gas, the gradient in the radial turbulence-intensity pushes the particles towards the wall (turbophoresis). This effect is balanced by the diffusion associated with a gradient in the particle-concentration, and it leads to a high particle-concentration near the wall, Portela et al. (2002). In general, turbophoresis pushes particles towards regions of low turbulence-intensity (i.e. towards the walls), and when the particles reach the wall they cannot, on average, acquire enough energy to go back to a higher turbulence-intensity region, leading to a clustering of the particles near the wall.

For F_{var} the radial gradient of the radial-Reynolds-stress is larger at the bottom (largest wall-roughness), thus we expect turbophoresis to be stronger at the bottom than at the top. Also, at the bottom, gravity and turbophoresis are working in the same direction, while at the top they are counter-acting, making wall-clustering weaker at the top.

4.2. Particle-laden flow

We used spherical particles with a diameter of either 50 μm or 100 μm and a density of 1000 kg/m^3, simulating water drops in air. The size is chosen such that the free-fall velocity of the particles in air is of the same order of magnitude of the secondary-flow velocity in the simulation F_{var} ($V_{\mathrm{T},50} = 0.090$ m/s, $V_{\mathrm{T},100} = 0.348$ m/s and $U_{\mathrm{sf}} \approx 0.2$ m/s, Fig. 4b). The gravitational acceleration is set to 9.81 m/s^2. At the start of the computation

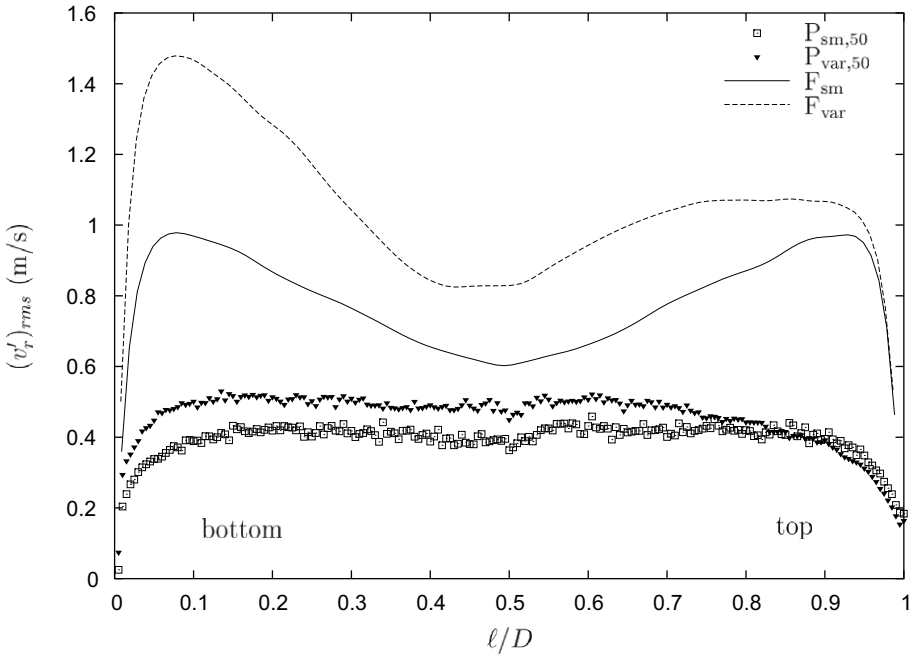

Fig. 5. Radial-velocity fluctuations at the vertical axis, for the simulations with and without secondary flow. The lines (F_{sm} and F_{var}) represent the values for the gas-phase and the symbols ($P_{sm,50}$ and $P_{var,50}$) the values for the 50 μm particles (the particles are discussed in Section 4.2).

800,000 particles were homogeneously distributed in the pipe (corresponding to a mean concentration of 1.63×10^9 m^{-3}), with zero slip-velocity. Four cases were considered:

- $P_{sm,50}$: 50 μm particles in a flow field with a smooth wall (F_{sm}),
- $P_{var,50}$: 50 μm particles in a flow field with a varying wall-roughness (F_{var}),
- $P_{sm,100}$: 100 μm particles in a flow field with a smooth wall (F_{sm}),
- $P_{var,100}$: 100 μm particles in a flow field with a varying wall-roughness (F_{var}).

Figs. 6 and 7 show some snapshots of the particle-distribution of the simulations $P_{sm,50}$ and $P_{var,50}$, respectively, for three instants in time: $t = 0$, $t = 0.5D/V_T$ and $t = D/V_T$. D/V_T is roughly the time that would take

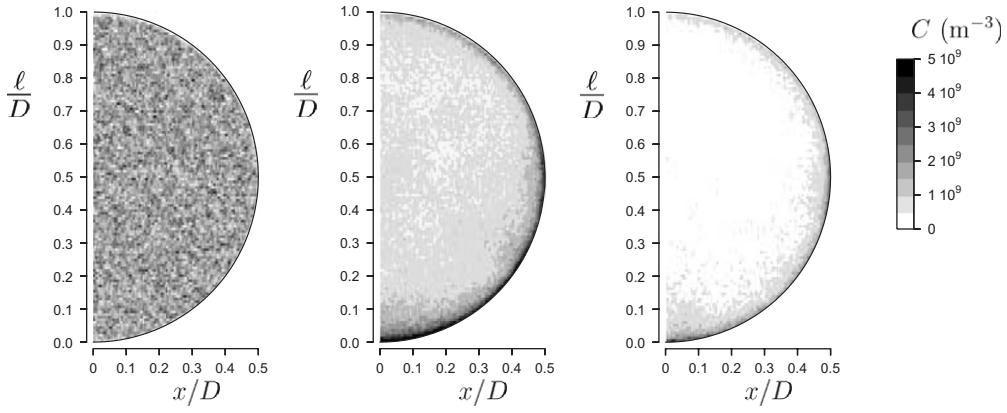

Fig. 6. Snapshots of particle-distribution in the pipe, for simulation $P_{sm,50}$, at three instants in time: $t = 0$, $t = 0.5D/V_T$ and $t = D/V_T$.

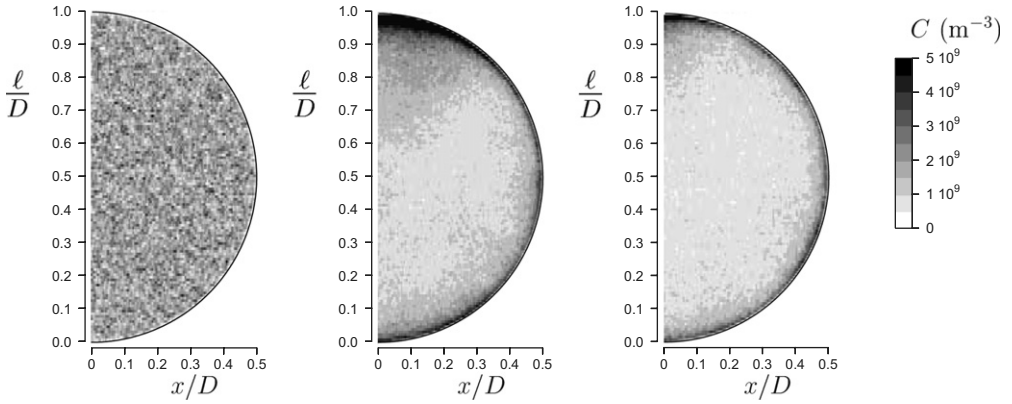

Fig. 7. Snapshots of particle-distribution in the pipe, for simulation $P_{\mathrm{var},50}$, at three instants in time: $t = 0$, $t = 0.5D/V_{\mathrm{T}}$ and $t = D/V_{\mathrm{T}}$.

for all the particles to deposit, if they would be moving in a stagnant medium. Both Figs. 6 and 7 show the rapid particle-depletion of the core region and the strong particle-accumulation at the wall. However, the particle concentration in the center of the pipe is larger for simulation $P_{\mathrm{var},50}$ than for simulation $P_{\mathrm{sm},50}$. Especially at the top region of the pipe, the secondary flow tends to mix the particles back into the core. The snapshots of the simulations $P_{\mathrm{sm},100}$ and $P_{\mathrm{var},100}$ are not shown here, since they show roughly the same trends.

Since in our simulations we are using a specular-reflecting wall, the particles do not actually deposit, but they bounce at the wall. When a particle hits the wall and bounces, this is treated as a single deposition-event. The results of the simulations show that the deposition-events can be divided into two different classes: (i) with active particles and (ii) with passive particles. The active particles are distributed throughout the pipe-volume and are in approximate equilibrium with the turbulence of the gas-phase. In contrast, the passive particles are concentrated in an 'accumulation region' close to the wall, due to turbophoresis, and they do not 'feel' the turbulence.

The results of the radial velocity of the particles, shown in Fig. 8, suggest that the accumulation-region can be defined as $y < D/200$. The active particles must have large radial-velocities, in order to be able to escape the accumulation-region after bouncing with the wall. On the other hand, the passive particles have small

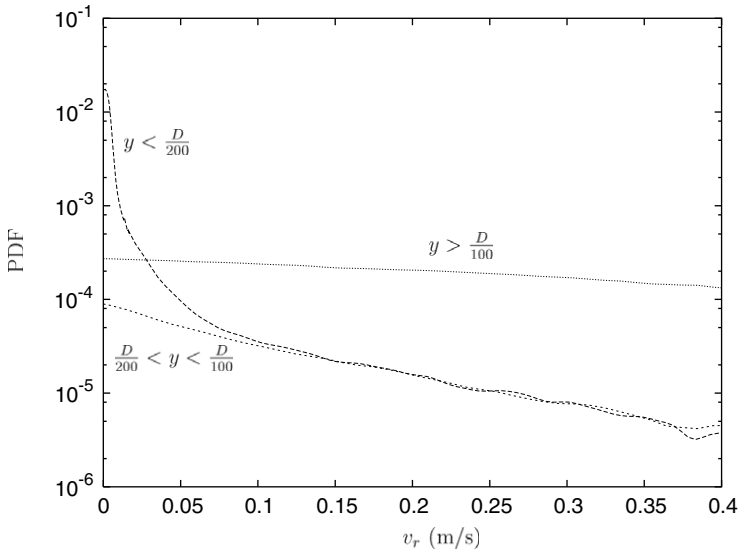

Fig. 8. Distribution of the positive radial-velocity of the particles in the accumulation-region ($y < D/200$), the 'mid'-region ($D/200 < y < D/100$), and the core-region ($y > D/100$), for $P_{\mathrm{sm},50}$ at $t = 0.5D/V_{\mathrm{T}}$.

radial-velocities and cannot escape the accumulation-region after bouncing with the wall (in essence, turbophoresis keeps them near the wall). In Fig. 8 we show the distribution of the positive radial-velocity of all the particles (both passive and active), for $P_{\mathrm{sm},50}$ at $t = 0.5D/V_{\mathrm{T}}$, separated into three different regions: the accumulation-region ($y < D/200$), the 'mid'-region ($D/200 < y < D/100$) and the core-region ($y > D/100$). The radial-velocity distribution for the accumulation-region shows a pronounced peak at small radial-velocities, which is absent in the mid and core regions. For radial-velocities larger than about 0.1 m/s, the distribution for the accumulation-region and the mid-region are similar. This indicates that the passive particles, with small radial-velocities, are located in the accumulation-region. Therefore, we define the deposition-events by passive particles as those for which the impact-velocity is below a threshold-velocity, $v_{\mathrm{min}} = 0.1$ m/s.

During the simulation, particles originally in the active class become trapped near the wall, and then belong to the passive class; turbophoresis may be the major contributor to this process. Since the passive particles are not expected to be representative for the dispersed phase of an actual annular flow, we are interested in the active particles only. The concentration of the active particles, C, decreases during the simulation, therefore, so does their rate of deposition at the wall, R_{D}. However, a quasi-steady situation is reached, in the sense that the deposition constant, $k_{\mathrm{D}} = R_{\mathrm{D}}/C$, does not change in time and the rate of deposition becomes proportional to the concentration of active particles, leading to an exponential-decay in the number of active particles. From Fig. 9, we see that for $t \gtrapprox 0.25D/V_{\mathrm{T}}$ there exists a large interval of time during which this quasi-steady situation is occurring. Further results on snapshots are presented for a particular time during this interval ($t = 0.5D/V_{\mathrm{T}}$) where the quasi-steady situation is already well-established and the concentration of active particles is still high.

Fig. 10 shows the concentration profile of the active particles on the vertical axis, $x = 0$ (lines), and near the wall, $y = 0.05D$ (symbols), for $P_{\mathrm{sm},50}$ and $P_{\mathrm{var},50}$, at $t = 0.5D/V_{\mathrm{T}}$. For $P_{\mathrm{sm},50}$, the concentration in the center of the pipe, $0.2 < \ell/D < 0.8$, decreases roughly exponentially with the vertical distance to the bottom, due to gravitational settling; i.e., a classical Rouse profile is found: $C \propto C_B \exp(-\beta\ell)$ with $\beta = 0.7$ as a fit parameter. Turbophoresis plays a dominant role near the wall, $y < 0.1D$, and causes the strong increase of concentration in this region; the concentration near the wall (symbols) is in general larger than the bulk concentration. We observe the particle-concentration in a horizontal plane, i.e. at a given value of ℓ, to be fairly constant in the center of the pipe, corresponding to a Rouse-profile.

The concentration of the active particles for simulation $P_{\mathrm{var},50}$ is larger than for $P_{\mathrm{sm},50}$, this difference becoming more pronounced with time, as can be seen in Figs. 6 and 7. A possible cause is that secondary flow

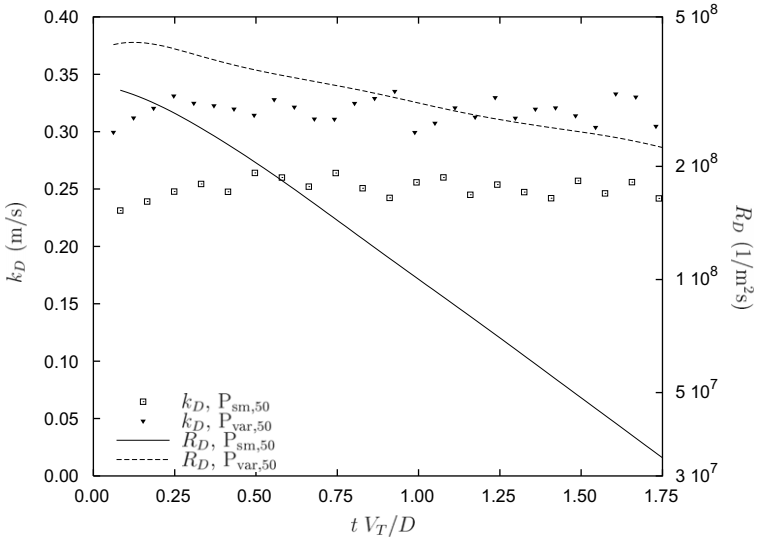

Fig. 9. Evolution in time of the deposition-constant and the rate of deposition at the wall, for $P_{\mathrm{sm},50}$ and $P_{\mathrm{var},50}$ (average values over the wall).

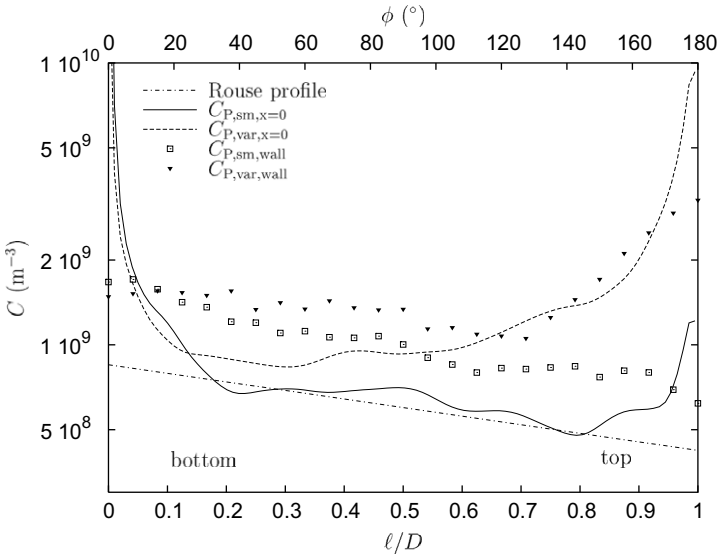

Fig. 10. Concentration profile of the active particles along the vertical axis, $x = 0$ (lines), as a function of the vertical distance to the bottom wall, ℓ (bottom axis), for $P_{sm,50}$ and $P_{var,50}$, at $t = 0.5D/V_T$. The dash-dotted line is a fit of a Rouse-profile to $P_{sm,50}$. The concentration near the wall, $y = 0.05D$ (symbols), is plotted as a function of the angle, ϕ (top axis). Since the results of $P_{sm,50}$ and $P_{var,50}$ are shown as a snapshot, the exact value of the concentration of the different simulations should not be compared directly.

is able to increase the velocity with which the particles impact at the wall, thus making the transition of a particle from the active to the passive class more difficult, so the concentration of active particles remains higher. Also, the secondary flow tends to 'mix' the particles more efficiently from the near-wall region into the core of the pipe, therefore increasing the number of active particles in the core of the pipe for $P_{var,50}$. The combination of a large concentration of active particles at the top-wall, and an effective transport of particles from the top-wall to the bottom wall through the center, by secondary flow, tends to increase the concentration at the top-half of the pipe, resulting in a plume-like concentration-pattern in the top region of the pipe, Fig. 7. This mixing-effect destroys the Rouse-profile for simulation $P_{var,50}$; the particle-concentration profile is more uniform, and even slightly increasing with ℓ in the center of the pipe, Fig. 10. The near-wall concentration of $P_{var,50}$, however, shows a remarkable inflection at $\phi = 130°$. The position of the inflection appears to be linked with the maximum magnitude of the secondary-flow velocity, and the sweeping of the particles by the centrifugal effects of the secondary-flow cells (Fig. 4b). The turbophoresis effect is present as well, shown by the strong increase in the concentration near the wall.

The concentration profile of the active particles in the pipe, especially the near-wall concentration, has a strong impact on the deposition-rate along the wall. In Fig. 11 we plot the local rate-of-deposition of the active particles, for $P_{sm,50}$ and $P_{var,50}$, at $t = 0.5D/V_T$. The deposition-rate of simulation $P_{sm,50}$ is larger at the bottom-wall than at the top-wall, mainly due to the differences in particle-concentration. Since the average concentration for $P_{var,50}$ is larger than for $P_{sm,50}$, the average particle-deposition-rate is larger as well. For $P_{var,50}$, the deposition-rate along the circumference, going from the bottom to the top of the tube, shows a smaller decrease than for $P_{sm,50}$. In simulation $P_{var,50}$, for $\phi \gtrapprox 130°$ the deposition-rate shows an abrupt increase, similarly to the near-wall concentration.

4.2.1. Free-flight model

Besides the concentration of the active particles, the deposition 'constant' is also an important factor in the rate of deposition, $R_D = k_D C$. Due to the circumferential variation of the radial-component of gravity, the deposition 'constant' varies as well. We consider here that k_D depends only on the turbulence and gravity, and use the free-flight model of Pan and Hanratty (2002) to understand the variation of k_D along the circumference. Note that, even though the turbophoresis effect is present in our simulations, their model does not explicitly use this mechanism, but it uses the average effect of the turbulence.

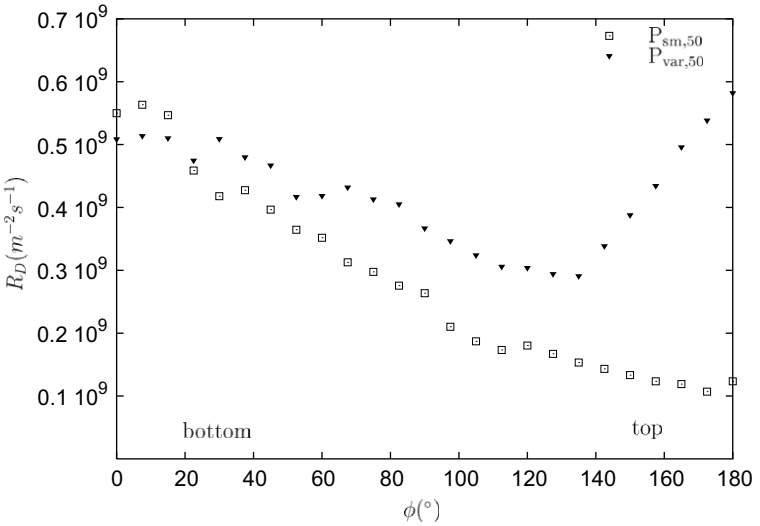

Fig. 11. Local rate-of-deposition, R_D, of the active particles, for simulations $P_{sm,50}$ and $P_{var,50}$, at $t = 0.5D/V_T$.

First, we discuss briefly their model, in which secondary flow is not considered, and compare it with the simulations. The parameters of their model can be estimated using submodels for C_D (Eq. (11)) and for σ_p, or can be viewed as tuning parameters for a parameter-fit of the results of the simulation to the model. The parameters of the model of Pan and Hanratty obtained by the parameter-fit are indicated with the superscript $*$.

In the model of Pan and Hanratty, it is assumed that all depositing particles start a free-flight to the wall from outside the viscous wall-layer. The radial-velocity distribution of the particles at the position where free-flight begins is assumed Gaussian, with a mean value equal to the terminal free-fall velocity projected onto the wall-normal, and a standard deviation σ_p; i.e., the PDF of the radial-velocity of the particles is assumed equal to

$$p(v_{p,r}) \propto \exp\left(-\frac{1}{2}(v_{p,r} - V_T\cos(\phi))^2/\sigma_p^2\right) \tag{14}$$

The local deposition-constant then becomes

$$k_D(\alpha) = \int_0^\infty v_{p,r}p(v_{p,r})\,dv_{p,r} = \frac{\sigma_p}{\sqrt{2\pi}}[\exp(-\alpha^2) + \sqrt{\pi}\alpha(1+\mathrm{erf}(\alpha))] \tag{15}$$

$$\alpha = \frac{V_T\cos(\phi)}{\sqrt{2}\sigma_p} \tag{16}$$

The variation of k_D along the pipe circumference is thus determined only by the ratio of the terminal free-fall-velocity and the velocity fluctuations of the particles (given by σ_p); this is shown in Fig. 12. For $V_T/\sigma_p \gtrapprox 3$, the deposition is dominated by gravity, $\langle k_D\rangle_\phi = V_T/\pi$. For $V_T/\sigma_p \lessapprox 0.1$, the deposition is dominated by the turbulence, $\langle k_D\rangle_\phi = \sigma_p/\sqrt{2\pi}$. For $0.1 \lessapprox V_T/\sigma_p \lessapprox 3.0$, there exists a competition between turbulence-deposition and gravitational-deposition.

Pan and Hanratty also assumed that the turbulence-intensity of the particles is equal throughout the whole pipe and that the dispersed phase is in equilibrium with the continuous phase, they assumed

$$\sigma_p^2 = \left(\frac{1}{1+0.7\tau_p/\tau_g}\right)(0.9u_\tau)^2 \tag{17}$$

$$\tau_g = 0.046D/u_\tau \tag{18}$$

where τ_g is the Lagrangian time-constant characterising the gas-phase turbulence.

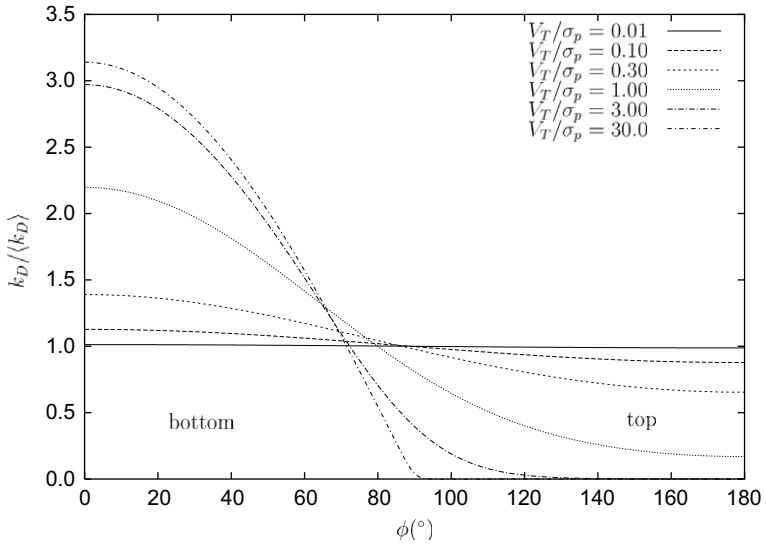

Fig. 12. Variation of the deposition 'constant' along the pipe circumference in a horizontal pipe, normalised with the mean deposition-constant, $\langle k_D \rangle$, according to Pan and Hanratty (2002).

4.2.2. Effect of secondary flow

We adopt the same approach and assume a single value for the gas-phase turbulence intensity for the whole flow field (i.e. we do not take into account the velocity-fluctuation change along the circumference due to the variation in wall-roughness).

Using the results of our simulation, the evaluation of $k_D = R_D/C$ can be done using the rate of deposition at the wall and the concentration. The deposition rate of the active particles at a given time is computed by averaging over a time-span of 10^{-2} s. The threshold velocity, $V_{min} = 0.1$ m/s, is used to distinguish the active from the passive depositing particles.

The concentration that we use for computing k_D is the free-flight concentration, C_{FF}, taken at the position where the active particles start their free-flight, y_{FF}. Note that, even though for all the deposition events the radial-velocity is positive, for the computation of the free-flight concentration, we use particles with both positive and negative radial-velocities.

In the central region of the pipe, the magnitude of the radial-velocity fluctuation of the active particles is roughly uniform. Near the wall, the gradient in the radial-velocity fluctuation of the continuous-phase is very steep, leading to a steep decrease in the radial-velocity fluctuation of the active particles. From Fig. 5, it appears that for $P_{sm,50}$ the near-wall decrease in the radial-velocity fluctuation of the active particles starts at $y/D = 0.05$ ($y^+ = 165$), which coincides, roughly, with the position of the maximum radial-velocity fluctuation of the continuous-phase. Here, we define the wall-distance where the free-flight starts as $y_{FF}/D = 0.05$, since the gradient in the radial-velocity fluctuation of the continuous-phase becomes very large closer to the wall, and the particles are not in equilibrium with the turbulence anymore (free-flight). The free-flight concentration thus becomes: $C_{FF} = C_{y/D=0.05}$. Since the near-wall decrease in the radial-velocity fluctuation of the active particles starts also at approximately the same location for $P_{var,50}$, $P_{sm,100}$ and $P_{var,100}$, we use the same definition for y_{FF} and C_{FF} for all the simulations.

For $P_{sm,50}$, we estimate the radial-velocity fluctuation of the active particles, σ_p^*, using Fig. 5 and taking the average value for $y/D > 0.1$. We determine the mean deposition-constant, $\langle k_D^* \rangle$, using Fig. 9 and taking the average value for $0.3D/u_\tau \lessapprox t \lessapprox 1.2D/u_\tau$. Then, the k_D-curve (Eq. (15)) is fitted to the local deposition-constant, normalised with the mean deposition-constant, and the tuning parameter V_T^*/σ_p^* is adjusted in order to get the 'best-fit' (least squares). The result is shown in Fig. 13. With the estimate of σ_p^* and V_T^*/σ_p^*, we determine the free-fall velocity, V_T^*. Note that, contrary to V_T, V_T^* is not a property of the particles; it is a best-fit tuning-parameter for the model of Pan and Hanratty. For the other simulations we used a similar procedure. The results of the fit are given in Table 1.

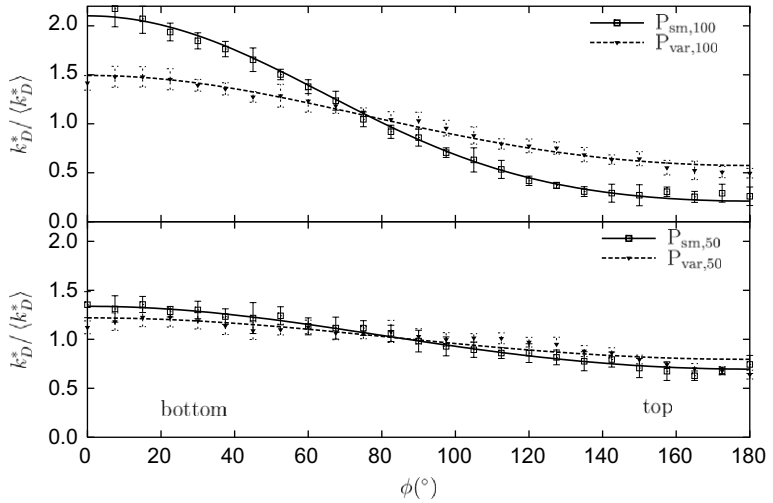

Fig. 13. Local deposition-constant normalised with the mean deposition-constant for simulations $P_{sm,50}$, $P_{var,50}$, $P_{sm,100}$ and $P_{var,100}$, using the fit parameters from Table 1. The averaging over multiple uncorrelated fields provides the mean (symbols) and the standard deviation ("error-bars") of the local deposition-constant.

Table 1
General results for all the simulations

	Model				Fit			
	V_T (m/s)	σ_p (m/s)	V_T/σ_p	$\langle k_D \rangle$ (m/s)	$\langle k_D^* \rangle$ (m/s)	V_T^*/σ_p^*	σ_p^* (m/s)	V_T^* (m/s)
$P_{sm,50}$	0.09	0.46	0.20	0.19	0.25	0.26	0.41	0.11
$P_{var,50}$	0.09	0.55	0.16	0.22	0.32	0.17	0.48	0.08
$P_{sm,100}$	0.35	0.26	1.34	0.15	0.19	0.90	0.24	0.22
$P_{var,100}$	0.35	0.31	1.14	0.16	0.20	0.38	0.28	0.11

Columns 2–5 are calculated using the model of Pan and Hanratty (2002). Columns 6–9 are parameter-fits of the results of the simulations to the model.

From Fig. 13 we observe that the fitted deposition constant, k_D^*, becomes more uniform (smaller V_T^*/σ_p^*) when secondary-flow is present. Since k_D^* is already quite uniform for $P_{sm,50}$, the effect is less pronounced for the simulations with the 50 μm particles. It should be noted that for $V_T^*/\sigma_p^* > 3$ or $V_T^*/\sigma_p^* < 0.1$ the fit of Eq. (15) becomes more difficult, since the shape of the curve hardly changes with V_T/σ_p; see Fig. 12.

From Table 1, we see that the model of Pan and Hanratty underestimates the deposition-constant for all the simulations; the largest discrepancy being with the 50 μm particles. Still, their model is able to give a reasonable prediction of the deposition-constant, and correctly predicts that the 50 μm particles have a larger deposition-constant than the 100 μm particles.

Probably, the most important cause for the difference in $\langle k_D \rangle$ between the model and the fit of the simulations is the determination of the free-flight concentration. Taking a start-position of free-flight, y_{FF}, too far away from the wall, results in a too small free-flight concentration, C_{FF}, since concentration decreases with distance from the wall. Hence the deposition constant will be overestimated. It thus seems that y_{FF} should be smaller than $0.05D$, since this will increase C_{FF}, and thus decrease $\langle k_D^* \rangle$. The difficulty in evaluating C_{FF} is a general problem of free-flight models. In the literature, the wall-distance where free-flight starts (stopping distance), usually is defined as, Friedlander and Johnstone (1957)

$$y_{FF} = v_{FF}\tau_p \tag{19}$$

where v_{FF} is a characteristic velocity of the particles moving towards the wall. The average positive-radial-velocity in $P_{sm,50}$ is equal to 0.5 m/s. Using this value for v_{FF} would result in $y_{FF}/D = 0.09$; i.e., y_{FF} would be larger than the value we used, leading to an even larger value of $\langle k_D^* \rangle$.

From Fig. 5, we see that the magnitude of the radial-velocity fluctuation of the particles is fairly constant in the central region of the pipe; it only decreases near the wall. In the central region of the pipe, the radial-velocity fluctuation of the particles is in approximate equilibrium with the turbulence intensity of the gas-phase, as assumed in the model of Pan and Hanratty. However, the model of Pan and Hanratty (Eq. (17)) overpredicts the radial-velocity fluctuation of the particles by about 10% for all the simulations. The overprediction of σ_p has two effects (see Eq. (15)): (i) by itself leads to an overall increase in k_D and (ii) combined with V_T promotes a change in α, leading to a change in the variation of k_D along the wall.

Nevertheless, the model of Pan and Hanratty predicts correctly the enhanced deposition at the bottom due to the gravity, and shows that this effect is stronger for the larger particles. Moreover, the variation of the deposition-rate along the wall can be well-fitted with the model. However, the fitting-parameter V_T^*/σ_p^* differs from the value of V_T/σ_p. For the 50 μm particles V_T^*/σ_p^* is higher than V_T/σ_p, whereas for the 100 μm particles it is lower. The value of V_T^* obtained from the fitting of the model to the results of the simulations is quite different from V_T, which is the terminal free-fall velocity of the particles in a stagnant medium. It is well known that the fall velocity of particles in a turbulent medium differs from the free-fall velocity in a stagnant medium (e.g. Davila and Hunt (2001)). Therefore, the model could be improved by considering the effect of the turbulence on the free-fall velocity of the particles.

The simulations with secondary flow have a variable wall-roughness and thus the turbulence intensity is larger. Due to the larger turbulence intensity, the radial-velocity fluctuation of the particles and the deposition-constant are larger. Also, with the increased turbulence intensity the gravitational contribution to the deposition becomes less dominant, resulting in a more uniform deposition along the wall. The model of Pan and Hanratty is able to predict the effects due to the larger turbulence intensity. For both the 50 μm and the 100 μm particles, the radial-velocity fluctuation of the particles is about 20% larger for the simulations with a variable wall-roughness than for the simulations with a smooth wall, and this is well predicted by the model; i.e., for both particle-diameters, σ_p and σ_p^* are about 20% larger with secondary flow. Therefore, the presence of secondary flow by itself does not seem to have a large influence on the radial-velocity fluctuation of the particles. The increase in the radial-velocity fluctuation of the particles appears to be mostly due to the increase in the turbulence intensity associated with the wall-roughness present in the secondary flow simulations. The more uniform deposition along the wall promoted by a larger turbulence intensity is also taken into account by the model of Pan and Hanratty, through the decrease in V_T^*/σ_p^* promoted by the increase in σ_p^*.

However, the value of V_T^*/σ_p^* that follows from the fit of the simulations is much smaller than the value that results from the increase in σ_p^*. Apparently, the secondary flow promotes a decrease in the terminal free-fall velocity of the particles, V_T^*, along the wall, and this decrease leads to a much smaller value of V_T^*/σ_p^*. Especially for the 100 μm particles, the effect of the secondary flow on the terminal free-fall velocity is quite dramatic: the value of V_T^* with secondary flow is half the value of V_T^* without it. A smaller terminal free-fall velocity results in a weaker gravitational settling, keeping the particles in the core of the pipe for a longer time, which leads to a larger particle-concentration, Fig. 10, and a larger rate of deposition, Fig. 11. Also, with a weaker gravitational settling the deposition becomes more uniform along the wall, Fig. 13. Clearly, an important improvement in the model of Pan and Hanratty would be to include the effect of the secondary flow on the fall-velocity of the particles.

Also the inclusion of circumferential variation of the gas-phase turbulence and the effects of turbophoresis may improve the model to describe the simulations. It should be noted that in an actual annular flow the effect of turbophoresis might be less strong than in the present simulations. In our simulations the particles remain entrained by the turbulence. In an actual annular flow the particles (droplets) deposit in the film and are ejected with a velocity that is not necessarily related with the local turbulence. Therefore, the turbulence has a smaller role in determining the near-wall behaviour of the particles, which might lead to a weakening of the turbophoresis effect. A possible way of including this effect is to use more realistic boundary conditions.

5. Conclusion

In this paper, a horizontal annular dispersed pipe flow is simulated using LES, with air and water being the gas and liquid phases. The turbulent gas-core is solved with an in-house code, using a bulk velocity of 20 m/s and a pipe diameter of 5 cm. The thin liquid-film is modeled as a cylindrical wall with a varying wall-roughness;

the bottom-wall being rough, $k_s/D = 0.03$, and the top-wall of the pipe being smooth, $k_s/D = 0$. The dispersed phase is simulated using a monodispersion of solid spheres, with a diameter of either 50 μm or 100 μm, driven by drag and gravity. Besides simulations with a varying wall-roughness, we also perform simulations with uniform roughness and with a smooth wall.

In modeling wall-roughness in turbulent single phase pipe flow, it is shown that the Schumann wall-function can be used: the law of the wall is well-resolved and there is good agreement with experiments from the literature. When the roughness is varied around the pipe wall, the pressure drop is well-predicted by averaging the friction-factor over the wall, so that every roughness-element contributes equally to the total wall-shear; also, the secondary-flow pattern agrees well with the measurements from Darling and McManus (1968).

In horizontal particle-laden pipe flows the particles are pushed towards the wall by the turbophoresis and towards the bottom by the gravity. This leads to a quick depletion of particles (droplets) in the core of the pipe. Our results indicate that the secondary flow induced by the variable film-thickness can have a large effect on the particle distribution and their deposition at the wall. The major global effect of the secondary flow is to bring the particles from the wall region to the core of the pipe, and, in particular, to the top part of the pipe. This increase in the particle-concentration in the core and top of the pipe leads to an overall increase in the rate of the deposition of the particles, which also becomes more uniform over the wall-circumference, with the rate of deposition at the top becoming of the same order of magnitude as the rate of deposition at the bottom. Besides this major global effect on the particle-concentration, the secondary flow induced by the variable wall-roughness can also promote changes in the deposition mechanisms themselves:

(i) Along the wall the secondary flow and gravitational settling act in opposite direction, therefore the presence of secondary flow reduces the relative importance of the settling with respect to the turbulence, making the deposition rate more uniform.
(ii) The wall-roughness leads to an increase in the overall turbulence intensity, increasing the overall deposition rate (due to an increase in the turbophoresis effect).
(iii) Due to the centrifugal effect of the secondary flow, the particles tend to be swept towards the wall, which can lead to a local increase in the rate of deposition in regions where the secondary flow velocity is larger.

All these changes in the deposition mechanisms are present and can play a significant role. However, our results indicate that the major effect of the secondary flow is through its influence on the redistribution of the particle-concentration.

The model of Pan and Hanratty (2002), based on the free-flight concept was used to fit the results of the deposition 'constant'. To compute the deposition 'constant', the concentration at the position where the free-flight starts is needed, and this can bring some uncertainty. Nevertheless, the model of Pan and Hanratty is able to predict the increase in the particle radial-velocity fluctuation and the higher and more uniform deposition-constant. Our results indicate that the effects of the secondary flow on the deposition rate could be incorporated into a simple model within the framework already developed by Pan and Hanratty. However, the model of Pan and Hanratty does not take into account the influence of both the turbulence and the secondary flow on the fall-velocity of the particles, and a significant improvement would be to include these effects.

Acknowledgements

This work is part of the research project: 'Liquid Loading in Inclined Pipes for Gas Production and Transport', sponsored by STW (Dutch Foundation for Technological Research). The code we use in the simulations is a modification of the single-phase solver for pipe flow with smooth walls written by Eggels (1994), at the Laboratory for Aero & Hydrodynamics from the Delft University of Technology.

Appendix A. Wall functions

In this appendix we validate the LES computations with wall-functions and verify the adequacy of the grid that we used. Also, we show that with a simple modification the Schumann wall-function for smooth walls can be used to simulate rough walls.

In order to validate the LES computations with wall-functions, a comparison is made with the experiments of Laufer (1954), Perry and Joubert (1963) and Zagarola and Smits (1998), for smooth walls. An averaging over the axial and tangential directions, and over multiple uncorrelated velocity fields (more than 100) was performed for simulations F_{sm} and F_{ro}. In Fig. A.1, the average axial-velocity is plotted as a function of the distance to the wall, in wall-units. Fig. A.2 shows the streamwise-velocity fluctuations and Fig. A.3 the radial-velocity fluctuations. Some flow properties for the different LES computations and the experimental data from literature are given in Table A.1.

Simulation F_{sm} agrees well with the mean axial-velocity profiles of Perry et al. and of Zagarola, but the measured data of Laufer are approximately 5% larger. For both F_{sm} and F_{ro} the logarithmic profile is nicely resolved and matches the law of the wall for a smooth and rough wall (dash-dotted). The axial-velocity fluctuations of F_{sm} and F_{ro} are in between the measurements of Laufer and Perry, but closer to the experiments of

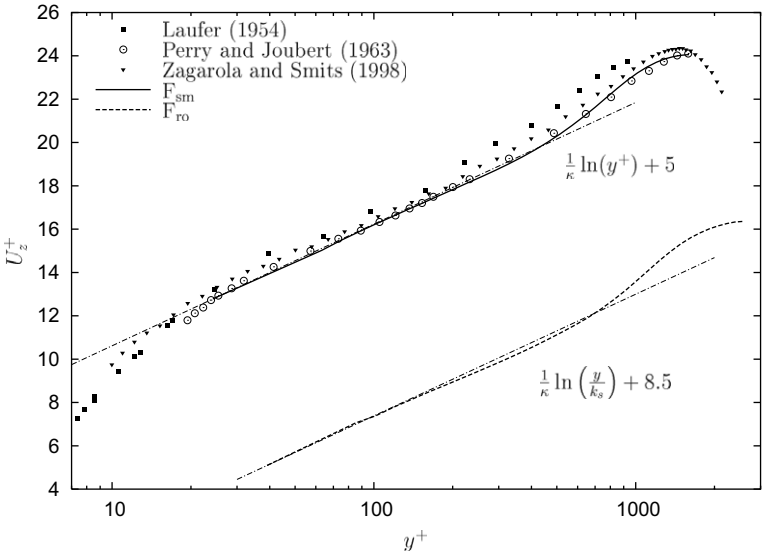

Fig. A.1. Mean axial-velocity profile.

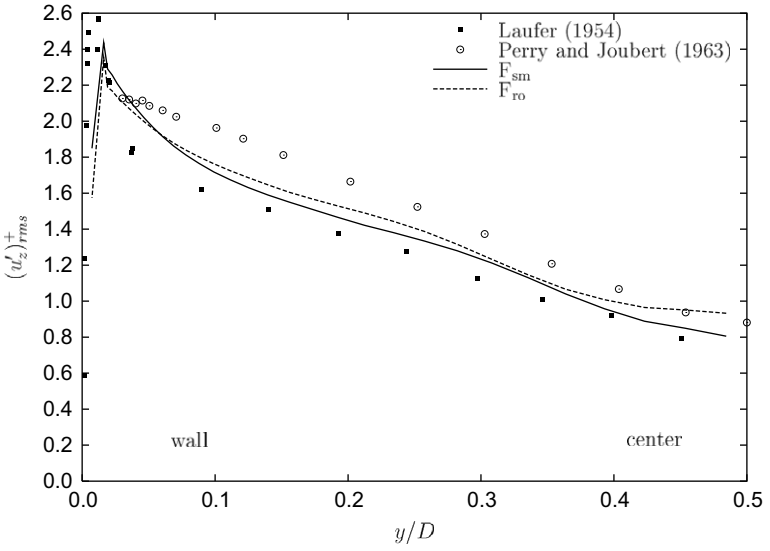

Fig. A.2. Axial-velocity fluctuations of the experiments of Perry and Joubert (1963), Laufer (1954), and simulations F_{sm} and F_{ro}.

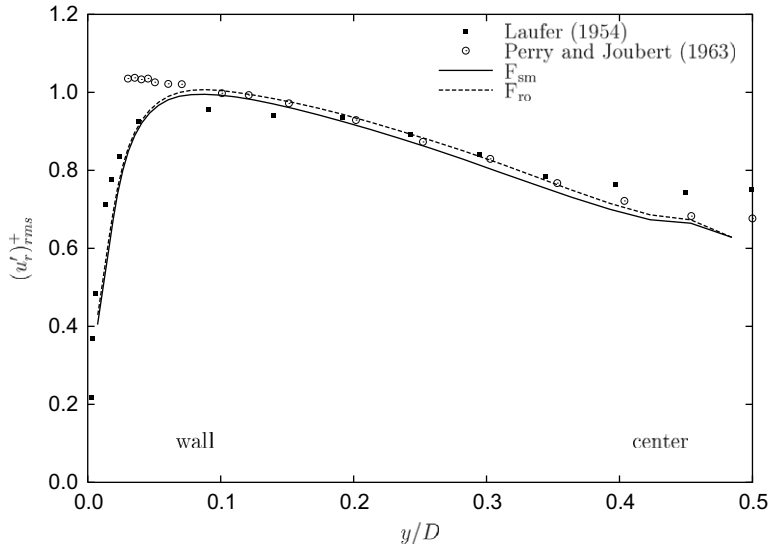

Fig. A.3. Radial-velocity fluctuations of the experiments of Perry and Joubert (1963), Laufer (1954), and simulations F_{sm} and F_{ro}.

Table A.1
Results for the continuous-phase of the simulations F_{sm} and F_{ro}, and the experiments of Laufer (1954), Perry and Joubert (1963), Zagarola and Smits (1998) and Darling and McManus (1968)

	U_{bulk} (m/s)	Re_{bulk}	Re_τ	f
Laufer	2.4	38,800	2060	0.0056
Perry	–	75,000	–	–
Zagarola	8.4	56,677	2860	0.0051
F_{sm}	19.60	65,300	3300	0.0051
F_{ro}	19.21	64,000	5274	0.0135

All the experiments used air and smooth walls.

Laufer. Note that the maximum in the axial-velocity fluctuations is not resolved in our simulations, since the first grid point is located at $y^+ = 24$ for F_{sm}, and at $y^+ = 39$ for F_{ro}.

The radial turbulence-intensity in the center of the pipe, agrees well with the measurements of both Laufer, and Perry and Joubert. We can conclude that the radial turbulence intensity is resolved with wall-functions, showing minima near the wall and in the center, and a maximum at $y/D \approx 0.07$ ($y^+ \approx 300$).

When implementing the Schumann wall-function (Eqs. (4)–(8) see, e.g., Piomelli et al., 1989), it is implicitly assumed that the instantaneous wall-shear-stress is proportional to the axial-velocity at the wall-nearest cell. Also, the near-wall turbulence structures (e.g., streaks) and events (e.g., bursts) are not resolved. Therefore, LES is not expected to give exact results for the two wall-nearest gridpoints for first-order statistics. Nevertheless, comparing the friction coefficient of F_{sm} with Blasius' relation, results in a mismatch of only 3.4%.

References

Belt, R.J., van 't Westende, J.M.C., Portela, L.M., Mudde, R.F., Oliemans, R.V.A., 2004. Particle-driven secondary flow in turbulent horizontal pipe flow. In: 3rd Int. Symp. on Two-Phase Modelling and Exp., Pisa, Italy. ISBN 88-467-1075-4.

Belt, R.J., van 't Westende, J.M.C., Portela, L.M., Mudde, R.F., Oliemans, R.V.A., 2005. Direct numerical simulation of particle-driven secondary flow in turbulent horizontal pipe flows. In: 11th Workshop on Two-Phase Flow Predictions, Merseburg, Germany. ISBN 3-86010-767-4.

Churchill, S.W., 1977. Friction factor equation spans all fluid flow regimes. Chem. Eng. 84.

Darling, R.S., McManus, H.N., 1968. Flow patterns in circular ducts with circumferential variation of roughness: a two-phase analog. Develop. Mech. 5, 153–170.

Davila, J., Hunt, J.C.R., 2001. Settling of small particles near vortices and in turbulence. J. Fluid Mech. 440, 117–145.
Dykhno, L.A., Williams, L.R., Hanratty, T.J., 1994. Maps of mean gas velocity for stratified flows with and without atomization. Int. J. Multiphase Flow 20, 691–702.
Eggels, J.G.M., 1994. Direct and large-eddy simulation of turbulent flow in a cylindrical pipe geometry. PhD thesis, Laboratory for Aero & Hydrodynamics, Delft University of Technology, 1994.
Flores, A.G., Crowe, K.E., Griffith, P., 1995. Gas-phase secondary flow in horizontal, stratified and annular two-phase flow. Int. J. Multiphase Flow 2, 207–221.
Friedlander, S.K., Johnstone, H.F., 1957. Deposition of suspended particles from turbulent gas streams. Ind. Eng. Chem. 49, 1151–1156.
Govan, A.H., 1989. A simple equation for the diffusion coefficient of large particles in a turbulent gas flow. Int. J. Multiphase Flow 15, 287–294.
Jayanti, S., Hewitt, G.F., 1996. Response of turbulent flow to abrupt changes in surface roughness and its relevance in horizontal annular flow. Appl. Math. Model. 20, 244–251.
Jayanti, S., Wilkes, S., Clarke, N.S., Hewitt, G.F., 1990. The prediction of turbulent flows over roughened surfaces and its application to interpretation of mechanism of horizontal annular flow. Proc. Roy. Soc. Lond. A 431, 71–88.
Jimenez, J., 2004. Turbulent flows over rough walls. Ann. Rev. Fluid Mech. 36, 173–196.
Laufer, J., 1954. The structure of turbulence in fully developed pipe flow. NACA Rep. 1174, 417–434.
Lin, T.F., Jones, O.C., Lahey, R.T., Block, R.T., Murase, M., 1985. Film thickness distribution for gas–liquid annular flow in a horizontal pipe. Physicochem. Hydrodyn. 6, 179–195.
Mols, B., 1999. Particle dispersion and deposition in horizontal turbulent channel and tube flows. PhD thesis, Laboratory for Aero & Hydrodynamics, Delft University of Technology, 1999.
Pan, L., Hanratty, T.J., 2002. Correlation of entrainment for annular flow in horizontal pipes. Int. J. Multiphase Flow 28, 385–408.
Perry, A.E., Joubert, P.N., 1963. Rough-wall boundary layers in adverse pressure gradients. J. Fluid Mech. 17, 193–211.
Piomelli, U., Ferziger, J., Moin, P., Kim, J., 1989. New approximate boundary conditions for large eddy simulations of wall-bounded flows. Phys. Fluids A 1, 1061–1068.
Portela, L.M., Oliemans, R.V.A., 2002. Subgrid particle-fluid coupling evaluation in large-eddy simulations of particle-laden flows. In: Proc. ASME IMECE.
Portela, L.M., Oliemans, R.V.A., 2003. Eulerian–Lagrangian DNS/LES of particle–turbulence interactions in wall-bounded flows. Int. J. Numer. Meth. Fluids 43, 1045–1065.
Portela, L.M., Cota, P., Oliemans, R.V.A., 2002. Numerical study of the near wall behaviour of particles in turbulent pipe flows. Powder Technol. 125, 149–157.
Speziale, C.G., 1982. On turbulent secondary flows in pipes of non-circular cross-section. Int. J. Eng. Sci. 20, 863–872.
van 't Westende, J.M.C., Belt, R.J., Portela, L.M., Mudde, R.F., Oliemans, R.V.A., 2004. Interaction of particles with secondary flow in high Reynolds number horizontal pipe flow. In: 3rd Int. Symp. on Two-Phase Modelling and Exp., Pisa, Italy. ISBN 88-467-1075-4.
Williams, L.R., Dykhno, L.A., Hanratty, T.J., 1996. Droplet flux contributions and entrainment in horizontal gas–liquid flows. Int. J. Multiphase Flow 22, 1–18.
Young, J., Leeming, A., 1997. A theory of particle deposition in turbulent pipe flow. J. Fluid Mech. 340, 129–159.
Zagarola, M.V., Smits, A.J., 1998. Mean-flow scaling of turbulent pipe flow. J. Fluid Mech. 373, 33–79.